Intercomparison of the representations of the atmospheric chemistry of pre-industrial methane and ozone in earth system and other global chemistry-transport models

Richard G. Derwent[1,*], David D. Parrish[2], Alex T. Archibald[3,4] Makoto Deushi[5], Susanne E. Bauer[6,7], Kostas Tsigaridis[7,6], Drew Shindell[8], Larry W. Horowitz[9], M. Anwar H. Khan[10], Dudley E. Shallcross[10,11]

[1]*rdscientific, Newbury, Berkshire, RG14 6LH, United Kingdom.*

[2]*David D. Parrish, LLC, Boulder, Colorado, USA.*

[3]*Department of Chemistry, University of Cambridge, Lensfield Road, Cambridge, CB2 1EW, UK.*

[4]*National Centre for Atmospheric Science, UK.*

[5]*Meteorological Research Institute, Japan Meteorological Agency, Tsukuba, Japan.*

[6]*NASA Goddard Institute for Space Studies, New York, USA.*

[7]*Center for Climate Systems Research, Columbia University, New York, USA.*

[8]*Nicholas School of the Environment, Duke University, Durham, NC 27708, USA.*

[9]*NOAA Geophysical Fluid Dynamics Laboratory, Princeton, NJ, USA.*

[10]*Biogeochemistry Research Centre, School of Chemistry, University of Bristol, Cantock's Close, Bristol BS8 1TS, UK.*

[11]*Department of Chemistry, University of Western Cape, Robert Sobukwe Road, Bellville 7375, South Africa.*

* Corresponding author. rdscientific, Newbury, Berkshire, RG14 6LH, United Kingdom.

E-mail address: r.derwent@btopenworld.com (R.G.Derwent).

1. Introduction

Ozone (O_3) is an important atmospheric pollutant that causes impacts on human health and vegetation and is also an important radiatively active trace gas (Monks et al., 2015). Ozone plays an important role in driving the atmospheric chemistry of the troposphere (Levy, 1972). Tropospheric chemistry acts as a removal process for the oxides of nitrogen (NO_x),

carbon monoxide (CO), methane (CH_4), sulphur dioxide (SO_2) and a myriad of organic compounds (Crutzen, 1974). Tropospheric chemistry also acts as an O_3 source in the sunlit polluted boundary layer and throughout the lower atmosphere.

To quantify the radiative forcing by O_3 and hence is contribution to climate change, it is necessary to quantify the seasonal and spatial distributions of O_3 in both the pre-industrial and present-day periods. Because of the high chemical reactivity of O_3, the historic tropospheric O_3 concentrations cannot be recovered from ice cores in the same manner as carbon dioxide (CO_2) (Raynaud and Barnola, 1985), CH_4 (Etheridge et al., 1992) and nitrous oxide (N_2O) (Khalil and Rasmussen, 1988), for example. Quantification of both the pre-industrial and present-day O_3 distributions is possible using earth system models (ESMs) but observations to compare with the model calculations and guide their improvement are available only for the present-day. Such comparisons increase our confidence in the model-derived present-day O_3 distribution. But, since such comparisons are not possible for the pre-industrial atmosphere, we must rely on other approaches to examine the confidence that we can have in the model-derived pre-industrial O_3 distribution. Providing such an approach is the goal of our paper.

The description of the chemistry of the pre-industrial atmosphere in global chemistry-transport models is necessarily highly uncertain because of the paucity and representativeness of observational data to feed into global models. Reliance must therefore be placed on chemistry, deposition and transport schemes as well as on global emission inventories to correctly describe the transition in the atmospheric composition of the troposphere from pre-industrial times through to the present-day. This transition has been particularly marked in some of the trace gases that control the distribution of tropospheric O_3, such as CH_4, NO_x and many organic compounds. Wang and Jacob (1988) used a three-dimensional tropospheric chemistry model to investigate pre-industrial O_3 levels and describe some of the uncertainties and potential difficulties. Of particular importance in their study was the level of pre-industrial NO_x emissions. Many of these difficulties still remain after the intervening three decades (Archibald et al., 2020).

Tropospheric O_3 chemistry is highly complex and there are many areas of uncertainty in the global chemistry-transport models (CTMs) used for policy predictions and the support of policy development for global climate change. Revell et al., (2018) and Wild et al., (2020)

have explored the uncertainties in the predictions of present-day tropospheric composition arising from uncertainties in emissions, deposition and vertical exchange. Additionally, Newsome and Evans (2017) have considered uncertainties arising from the representation of atmospheric chemistry in the present-day atmosphere. In contrast, because there is a paucity of studies addressing uncertainties in the pre-industrial atmosphere, attention is focussed here on the uncertainties in the atmospheric chemistry of O_3 and CH_4 in the pre-industrial troposphere and its representation in global models. Global models have been the main tools for understanding the climate system and for predicting future climate change (IPCC, 1990; 1996; 2001; 2013). More recently, global climate models have incorporated atmospheric chemistry and biogeochemical processes, evolving into earth system models (Young et al., 2018; Sellar et al., 2019; Yukimoto et al., 2019). Earth system models (ESMs) are now recognised as the main tools for the prediction of the time evolution of the climate system, together with that of the distributions of all relevant radiatively-active trace gases and aerosols from the pre-industrial times through to the end of the century (IPCC, 2013).

In this study, an intercomparison has been set up to examine in detail the representation of the atmospheric chemistry of pre-industrial CH_4 and O_3 in six of the ESMs that took part in the sixth phase of the Coupled Model Intercomparison Project (CMIP6) (Eyring et al., 2016). The question is what are the likely levels of uncertainty in earth system model predictions of pre-industrial CH_4 and O_3 chemistry. We show that inter-model (or inter-mechanism) range is a poor predictor of likely uncertainty which is driven by the uncertainties in a small number of key reaction rate coefficients and reaction product yields.

2. Methods

2.1 The constrained box model

This intercomparison employed a constrained box-model approach that has previously been applied to the polluted boundary layer (Derwent, 2017) and to the background troposphere (Derwent, 2020). Here, the constrained box-model is focussed on the representation of the atmospheric chemistry of O_3 and CH_4 in the pre-industrial atmosphere and its representation in earth system and other global chemistry-transport models. The formulation of the constrained box-model was based on the Photochemical Trajectory Model (PTM), the details of which are given elsewhere (Derwent et al., 2010). In this

application, wet and dry deposition, exchange with the free troposphere and emission processes have been switched off, leaving the complete focus on the chemical development of O_3 and CH_4 and that of the hydroxyl (OH) radical species that drives it.

In a box model, a differential equation of the form:

$$dc_i/dt = P_i - l_i c_i \quad (1).$$

was set up for each model species, i, where c_i is the concentration of species, i, in the box, P_i is its production rate from chemistry and l_i is the first order loss coefficient arising from chemistry. In a constrained box model, the above differential equation is modified by the addition of a net flux, F_i, to the right-hand side of the equation so that the rate of change of the species, i, remains zero and its concentration remains constant at the constrained value, c_i*, listed in Table 2:

$$dc_i/dt = 0 = P_i - l_i c_i^* + F_i \quad (2).$$

The Gear's method automatic numerical integrator FACSIMILE (Curtis and Sweetenham, 1987) returns the flux, F_i, required at the end of each time step to maintain the concentrations of each species at its constraint. This flux is then integrated over a time period of 5 days to give the time-integrated production or loss flux (depending on its sign) for that species. The output of the constrained box model is therefore the time-integrated production or loss fluxes for each of the upwards of twenty-two constrained species. Particular focus was given in this study to the time-integrated ozone production flux, P_{O3}.

For the many species without constrained values, these species would reach some form of local instantaneous photochemical steady state and their diurnally-varying concentrations would be set by equations of the form of (1) above. Their concentrations were averaged over the 5-day time period and provided another set of outputs. Particular focus was given to the 5-day average hydroxyl radical number density, ($\underline{OH}$), together with those of the hydroperoxyl ($\underline{HO_2}$) and the methylperoxy ($\underline{CH_3O_2}$).

2.2 Chemical mechanisms employed in the intercomparison

Table 1 summarises the details of the eight chemical mechanisms studied, together with their supporting literature references. They varied in complexity from the highly detailed and explicit Master Chemical Mechanism (MCM) v3.3.1 (https://mcm.york.ac.uk) to the

condensed and parameterised mechanisms that are typically employed in earth system and other global models. The CESM2-WACCM and GFDL-ESM4 earth system models utilise chemical mechanisms which owe their origins to the MOZART family of mechanisms (Emmons et al., 2010; https://www2.acom.ucar.edu/gcm/mozart). UKESM1-0-LL and STOCHEM-CRI models employ mechanisms that are descended from the MCM, the BCC-GEOS-CHEMv1.0 from the GEOS-CHEM mechanism and the GISS-E2-1-H and the MRI-ESM2.0 from the Carbon Bond series of mechanisms (ENVIRON, 2005). Broadly speaking, rate coefficients for five mechanisms (BCC-GEOS-CHEMv1.0, CESM2-WACCM, GFDL-ESM4, GISS-E2-1-H and MRI-ESM2.0) are based on the JPL evaluated chemical kinetic data compilation (Burkholder et al., 2015) and for three mechanisms (STOCHEM-CRI, UKESM1-0-LL and MCMv3.3.1) on the IUPAC evaluation (Amman et al., 2013).

The mechanisms were, however, not implemented as published but were harmonised to minimise the influence of publication date. The first harmonisation addressed the so-called 'inorganic' chemistry. This set of close to fifty chemical reactions establishes the fast photochemical balance, involving the hydroxyl (OH), hydroperoxy (HO_2) and oxygen (O^1D and O^3P) atoms and their reactions with nitric oxide (NO), nitrogen dioxide (NO_2), ozone (O_3), water vapour, carbon monoxide (CO), hydrogen (H_2) and sulphur dioxide (SO_2). The 'inorganic' chemistry provided with each mechanism was removed and replaced with a set of 49 chemical reaction pathways and rate coefficients, together with their temperature and pressure dependences, taken from IUPAC (http://iupac.pole-ether.fr/) (Amman et al., 2013). By harmonising the 'inorganic' chemistry, we are not saying that the uncertainties in this chemistry are unimportant but merely that our present focus is on the $C_1 - C_3$ chemistry of CH_4 and O_3. Indeed, there have been several studies in the literature that point to the importance of 'inorganic chemistry as a source of uncertainty in chemistry-transport models (Newsome and Evans, 2017; Revell et al., 2018; Wild et al., 2019).

The second harmonisation involved the photolysis rate coefficients. All photolysis rate coefficients provided with each mechanism were replaced with a standard set taken from the MCM website (http://mcm.york.ac.uk/parameters/photolysis_parameters.htt) for present-day conditions. In particular, this harmonisation step applied to the photolysis rates for the aldehydes: formaldehyde (HCHO), acetaldehyde (CH_3CHO) and propionaldehyde (C_2H_5CHO), for the ketone: acetone (CH_3COCH_3) and for methyl hydroperoxide (CH_3OOH)

and the higher hydroperoxides (ROOH). In addition, some chemical mechanisms treated the photolysis of methyl nitrate (CH_3NO_3). By harmonising photolysis rate coefficients, we do not wish to convey the impression that photolysis rates are an unimportant source of model uncertainty but merely that our present focus is on the choice of thermal rate coefficients for the $C_1 – C_3$ chemistry used in earth system and other chemistry-transport models. Indeed, Hall et al., (2018) described a detailed comparison of the photolysis rates from nine chemistry-transport models (including several of those models whose chemical mechanisms are studied here) with aircraft measurements and showed the importance of the uncertainties in cloud impacts on tropospheric chemistry.

The final harmonisation involved the rate coefficients for the formation and decomposition of the peroxyacyl nitrates. Again, these were replaced with a standard set of rate coefficients, together with their pressure and temperature dependences taken from the MCM website (http://mcm.york.ac.uk/parameters/complex.htt). The remainders of each mechanism, particularly the reactions of CH_4, methylperoxy (CH_3O_2), methyl hydroperoxide (CH_3OOH), formaldehyde (HCHO) and those of ethane, propane and acetone were implemented exactly as laid out in the published details of the earth system or global chemistry-transport model. The details of the CH_4 chemistry and that of the other C_1 compounds implemented for each of the eight mechanisms are provided in Table S.1 of the Supplementary Information, for ethane and other C_2 compounds in Table S.2 and for propane and acetone in Table S.3.

It is understood that these harmonisation steps may well move the mechanisms away from the conditions and chemical regimes under which they were developed by their originators. This was considered inevitable. As a result, the performance of the mechanisms may be different from that if no changes had been made. Due to the nature of the intercomparison, no treatments were included of halogen or heterogeneous chemistry with any of the chemical mechanisms.

2.3 Background environmental conditions

Any intercomparison of chemical mechanisms needs input data on background environmental conditions to set up an appropriate chemical regime to frame the evaluation. In this study, output has been taken from STOCHEM-CRI (Derwent et al., 2015) for pre-

industrial conditions and was used to provide plausible meteorological and mixing ratios for a number of trace gases at ninety locations close to the surface spread for mid-July conditions. The chosen locations were in the tropics and temperate latitudes, sited on a 20^o latitude by 20^o longitude grid covering the latitude range from 37.5^o S to 42.5^o N and from 162.5^o E to 177.5^o W. By choosing locations spread over both hemispheres, we have automatically accounted for summer and winter photochemical conditions. The trace gases, of which there are twenty-two in all, see Table 2, included ozone precursors and reaction products with atmospheric lifetimes of the order of minutes and longer. Free radical species have much shorter lifetimes and were not set up in the same way but were allowed to establish their own levels based on the time-dependent photochemical activity in each of the constrained box model calculations.

One of the chemical mechanisms employed in one of the earth system models (GISS-E2-1-H) operated with a C_1-only chemistry and, in this respect, was quite distinct from the others. The other chemical mechanisms will have contributions to the number densities of CH_3O_2 from the oxidation of a range of C_2 – C_3 organic compounds, in addition to those from CH_4, methanol (CH_3OH) and methyl hydroperoxide (CH_3OOH). During the chemical mechanism testing and evaluation phase, this may influence the apparent performance of the mechanisms and may introduce bias into the intercomparison. Therefore, a much more simplified set of background environmental conditions was drawn up for the testing and evaluation phase. This simplified set of constraints addressed only CH_4, O_3, H_2, NO and NO_2 and the details are presented in the second column of Table 2 and considered only a single location.

In all other model experiments, the full set of 90 background locations were employed with the full range of trace gas composition data. The third column of Table 2 gives the range of variables calculated by STOCHEM-CRI at the ninety locations which are used to constrain the box model calculations.

2.4 Description of the Monte Carlo uncertainty analysis

There were three steps in our Monte Carlo assessment of uncertainties (Derwent et al., 2018) in the constrained box model predictions due to uncertainties in the input chemical kinetic data. In the first step, the constrained box model code was altered to accept a

multiplier for each model chemical kinetic input parameter, scaling the evaluated 'best estimate' values. In the second step, the uncertain input ranges for each parameter were sampled quasi-randomly and input values were set for the initialisation of each constrained box model run. In the third step, the constrained box model was run repeatedly a large number, typically 1,000, times with each run having a different random selection of chemical kinetic input parameters. Each constrained box model run returned the five-day time-integrated $\underline{OH}$, $\underline{HO_2}$ and $\underline{CH_3O_2}$ and the time-integrated fluxes through each chemical reaction. Because all other constrained box model inputs remained exactly the same, differences in the model outputs could be accurately discerned.

For each chemical kinetic input parameter selected for uncertainty analysis, 5 – 95 % (2 – σ) confidence ranges were established based on multiplicative scaling about the 'best estimate' values. The upper and lower values for these ranges were taken from the chemical kinetic data evaluations (Burkholder et al, 2015; Amman et al., 2013). Probability distributions within these ranges were taken to be equally distributed on either side of the best estimates', that is to say 'top hat' in shape (Derwent et al., 2018). A 'top hat' distribution was chosen because it is simple and straightforward. We note that Newsome and Evans (2017) adopted a 'normal' distribution whereas Revell et al., (2018) and Wild et al., (2019) adopted a 'top hat' distribution as here.

2.5 Testing and evaluating the constrained box model

The constrained box model was set up with each of the eight chemical mechanisms from the earth system and global models from Table 1 and the simplified set of background environmental conditions from the second column of Table 2 for a single location. For each chemical mechanism, the constrained box model was integrated for five days and the time-averaged net rate of O_3 (production – loss) required to maintain its constrained mixing ratio was noted. The instantaneous OH and HO_2 number densities averaged over the five-day period were also calculated and these three numbers for the eight chemical mechanisms are presented in Table 3.

Under the simplified background environmental conditions, the atmospheric chemistry was driven by the photolysis of O_3 to give excited oxygen atoms, which reacted with water vapour to produce OH:

$O_3 + hv \rightarrow O_2 + O^1D$

$O(^1D) + H_2O \rightarrow OH + OH.$

OH reacted predominantly with carbon monoxide (CO) to generate HO_2:

$OH + CO \rightarrow H + CO_2$

$H + O_2 + M \rightarrow HO_2 + M.$

HO_2 has a number of possible fates, including the regeneration of OH by:

$HO_2 + NO \rightarrow OH + NO_2$

$HO_2 + O_3 \rightarrow OH + O_2 + O_2.$

However, not all of the HO_2 reacted with NO or O_3, as some recombined to form hydrogen peroxide (H_2O_2):

$HO_2 + HO_2 + M \rightarrow H_2O_2 + O_2 + M.$

The HO_2 that recombined in this way, acted as a sink for free radicals. Consequently, about one quarter of the OH + CO reaction flux was recycled back to OH and three quarters acted as a sink for OH under the simplified background environmental conditions.

OH reacted with a wide range of trace gases in addition to CO. The reactions of OH with H_2 and O_3 acted in a similar manner as the OH + CO reaction by recycling a fraction of the OH through to HO_2. The reactions of OH with HO_2 and NO_2, however, acted as total sinks for OH since their reaction products did not recycle back to OH by way of HO_2:

$OH + HO_2 \rightarrow H_2O + O_2$

$OH + NO_2 + M \rightarrow HNO_3 + M.$

All of the reactions of OH, HO_2, H_2O_2, CO, H_2 and NO_x were included in the 'inorganic' reactions of the fast photochemical balance of the troposphere and their rate coefficients were standardised and harmonised to be identical within each of the eight chemical mechanisms studied.

The chemical mechanisms diverged in their treatment of the atmospheric chemistry of CH_4 and its C_1 reaction products following the reaction of OH with CH_4:

$OH + CH_4 \rightarrow CH_3 + H_2O$.

Methyl (CH_3) radicals rapidly reacted with molecular oxygen to produce CH_3O_2:

$CH_3 + O_2 + M \rightarrow CH_3O_2 + M$.

CH_3O_2 had a number of fates under tropospheric conditions:

$CH_3O_2 + NO \rightarrow CH_3O + NO_2$

$CH_3O_2 + HO_2 \rightarrow$ products

$CH_3O_2 + CH_3O_2 \rightarrow$ products.

The reaction of CH_3O_2 with NO produced methoxy (CH_3O) whose main fate was to react with oxygen to produce HO_2 and HCHO:

$CH_3O + O_2 \rightarrow HO_2 + HCHO$.

This reaction produced HO_2 which could then go on to react with NO or O_3 to regenerate the OH. In consequence, about one twentieth of the reaction flux through $OH + CH_4$ was recycled back to OH and the remainder acted as a sink for OH under the simplified background environmental conditions.

None of the rate coefficients defining the atmospheric chemistry of CH_4 and its C_1 reaction products were standardised or harmonised between the eight different chemical mechanisms, except for the photolysis reactions of HCHO and CH_3OOH. The chemical mechanism developers provided their own unique descriptions of the chemical processes involved, including rate coefficients and reactions products for the $CH_3O_2 + HO_2$ and $CH_3O_2 + CH_3O_2$ reactions. Any divergences in the base case model results for P_{O3}, $\underline{OH}$, $\underline{HO_2}$ and $\underline{CH_3O_2}$ necessarily stemmed wholly from any divergences in the representation of the atmospheric chemistry of CH_4 and its C_1 chemistry among the eight chemical mechanisms.

Overall, the results presented in Table 3 show a reasonable level of agreement, that is to say within ± 5%, across the three metrics and eight chemical mechanisms despite many apparent divergences in the representation of the CH_4 and C_1 chemistry illuminated in Table S.1. The inter-mechanism ranges for the P_{O3}, $\underline{OH}$ and $\underline{HO_2}$ metrics expressed as a fraction of the inter-mechanism average were 0.064, 0.071 and 0.10 as shown in Table 3. From this level of agreement for the three metrics, it was concluded that the harmonisation and

standardisation measures, together with the simplified background environmental conditions had ensured that all the chemical mechanisms have been implemented reasonably accurately within the constrained box model without the introduction of distortion or bias and with a reasonable level of conformity.

Having said that, there are small differences between the results for the different metrics and between the different chemical mechanisms, see Table 3, and it is important to offer some explanation for these differences. Across the three metrics, there was a tendency for the GISS-E2-1-H and UKESM1-0-LL mechanisms to generate results that lay towards the limits of the inter-mechanism ranges and hence the investigation of the divergences between the chemical mechanisms in Table 3 began with them.

Examination of the representation of C_1 chemistry in Table S.1 of the Supplementary Information indicated four minor differences between its implementation in GISS-E2-1-H and in the other earth system models. These involved the NO_3 + HCHO, OH + CH_3OOH, CH_3O_2 + CH_3O_2 and OH + CH_4 reaction rate coefficients. A series of one-at-a-time (OAT) sensitivity experiments was performed where each of the above rate coefficients were replaced with those from another earth system model (usually CESM2-WACCM). Three sensitivity experiments revealed trivial impacts from rate coefficient substitution but the sensitivity experiment involving the rate coefficient and product yields for OH + CH_3OOH was found to account for all of the underestimation of $\underline{OH}$ and $\underline{HO_2}$ and the overestimation of P_{O3} found with GISS-E2-1-H, see Table 3, when compared to the average of all model chemical mechanisms.

In an analogous manner, twelve differences were found in Table S.1 of the Supplementary Information between the implementation of the C_1 chemistry in the UKESM1-0-LL model compared with that in some of the other earth system models. OAT sensitivity tests revealed two differences that accounted for the whole of the apparent overestimation of $\underline{OH}$ and $\underline{HO_2}$ and the underestimation of P_{O3} shown in Table 3, relative to other model mechanisms. As with the GISS-E2-1-H model mechanism, these differences in UKESM1-0-LL both involved the OH + CH_3OOH reaction, through the choice of rate coefficient and the specification of the relative yields for the two reactive channels for this reaction.

It is also instructive to compare the predictions in Table 3 from the MCMv3.3.1 and STOCHEM-CRI since, although the results were very similar, they were not identical as expected. The P_{O3}, $\underline{OH}$ and $\underline{HO_2}$ differed by +0.47%, -0.77% and -0.78%, respectively. Detailed inspection of the chemical kinetic data employed in each chemical mechanism revealed two sets of differences, despite the application of the harmonisation and standardisation procedures. The first difference involved the inclusion in MCMv3.3.1 but not in STOCHEM-CRI of the formation and thermal decomposition of methyl peroxy nitrate ($CH_3O_2NO_2$). The second difference was the number of routes included for the $CH_3O_2 + HO_2$ reaction: two, as in MCMv3.3.1, or one, as in STOCHEM-CRI. OAT sensitivity tests revealed that the formation and decomposition of $CH_3O_2NO_2$ was entirely unimportant in terms of the four metrics in Table 3 under the simplified background environmental conditions as expected based on Khan et al., (2020) but that the implementation of the second minor route in $CH_3O_2 + HO_2$ forming HCHO accounted for all the differences between MCMv3.3.1 and STOCHEM-CRI.

In summary, all the differences in P_{O3}, $\underline{OH}$ and $\underline{HO_2}$ apparent in Table 3 can be accounted for by differences in the implementation of the two reactions: $OH + CH_3OOH$ and $CH_3O_2 + HO_2$ across the eight chemical mechanisms. Considering first the $OH + CH_3OOH$ reaction, then it is noted that the two major compilations of chemical kinetic data for atmospheric modelling purposes: IUPAC (Amman et al., 2013) and JPL (Burkholder et al., 2015), diverge significantly in their evaluations and recommendations for this reaction. Under the simplified environmental conditions, (see Table 2), the rate coefficients for the $OH + CH_3OOH$ reaction differ significantly: 1.00×10^{-11} cm^3 $molecule^{-1}$ s^{-1} in IUPAC and 7.47×10^{-12} cm^3 $molecule^{-1}$ s^{-1} in JPL. However, both evaluations quote wide uncertainty limits for this reaction, such that the differences between the evaluations are not significant. IUPAC and JPL quote uncertainty ranges of $(0.5 – 2.0) \times 10^{-11}$ cm^3 $molecule^{-1}$ s^{-1} and $(0.38 – 1.45) \times 10^{-11}$ cm^3 $molecule^{-1}$ s^{-1}, respectively. Furthermore, there are significant differences in the evaluations and recommendations for the branching ratios for the two routes for this reaction:

$OH + CH_3OOH \rightarrow HCHO + OH + H_2O$ (minor channel) and

$OH + CH_3OOH \rightarrow CH_3O_2 + H_2O$, (major channel).

These differences in evaluated and recommended chemical kinetic data have directly caused the discrepancies noted In Table 3, however, there is no clear basis by which to choose between the recommendations from the IUPAC and JPL data compilations for the OH + CH_3OOH reaction.

Considering the CH_3O_2 + HO_2 reaction, it is noted that the IUPAC (Amman et al., 2013) and the JPL (Burkholder et al., 2015) chemical data evaluations agree closely in their recommendations. However, both evaluations point to wide uncertainty ranges under the conditions of the simplified environmental conditions: (3.08 – 8.79) x 10^{-12} cm^3 $molecule^{-1}$ s^{-1} in JPL and (3.28 – 8.2) x 10^{-12} cm^3 $molecule^{-1}$ s^{-1} in IUPAC. They disagree about the importance of the minor reaction channel. The recommended yield for the minor channel:

CH_3O_2 + HO_2 → O_2 + HCHO + H_2O , versus the major channel:

CH_3O_2 + HO_2 → O_2 + CH_3OOH ,

is zero in JPL but is 0.1 in IUPAC. However, uncertainties are large and there is not a lot of difference between the evaluations. Removing the minor channel from the MCMv3.3.1 and STOCHEM-CRI, in agreement with the other mechanisms in Table S.1, accounted for all the differences seen in the three metrics in Table 3 between the MCMv3.3.1 and STOCHEM-CRI.

3. Application of the constrained box model to the impacts of NO_x in the pre-industrial atmosphere

The constrained box model was set up with a 'base case', using the pre-industrial background environmental conditions for CH_4, O_3, CO and H_2 from a STOCHEM-CRI simulation (Derwent et al., 2015) for each of the 90 gridded locations and for each chemical mechanism taken from the third column of Table 2. The constrained mixing ratios for NO and NO_2 were then reduced in 10% steps from their base case values and the P_{O3}, $\underline{OH}$, $\underline{HO_2}$ and $\underline{CH_3O_2}$ were noted. In addition, the time-integrated fluxes through each of the C_1 reactions in Table S.1 were monitored as the NO_x mixing ratios were reduced. It was found that the time-integrated fluxes through the O_3 source reactions:

HO_2 + NO → OH + NO_2, and

CH_3O_2 + NO → CH_3O + NO_2 , followed by

$CH_3O + O_2 \rightarrow HO_2 + HCHO$,

decreased step-wise in line with the NO_x mixing ratios and that those through the O_3 sink reactions:

$HO_2 + O_3 \rightarrow OH + O_2 + O_2$, and

$OH + O_3 \rightarrow HO_2 + O_2$,

also did likewise. The decrease in the reaction flux through the O_3 sink reactions thus acted as an apparent increase in the net O_3 source. However, with all the chemical mechanisms, the decrease in the fluxes through O_3 sinks was not enough to compensate for the decrease in the fluxes through O_3 sources and so the net rate of O_3 production decreased in step with the decrease in the NO_x mixing ratios. At some point with the decreasing NO_x mixing ratios, the net rate of O_3 production changed sign from net production to net loss. This point is the NO_x compensation point.

The NO_x compensation points found at each of the 90 background troposphere locations varied from just below 10 ppt to just below 70 ppt, with an average of 24 ± 12 ppt with MCMv3.3.1. The spatial patterns of the variations in compensation points across the 90 locations were closely similar between the different chemical mechanisms and were driven largely by the spatial pattern in the O_3 mixing ratios in the background environmental conditions. As the background O_3 mixing ratio increased from 7.4 ppb to 20.6 ppb, the NO_x compensation point increased from 9.3 ppt to 68 ppt with MCMv3.3.1. Scatter plots of the compensation points found with MCMv3.3.1 versus the other seven mechanisms were closely linear ($R^2 > 0.97$) and are presented in Figure S.1 in the Supplementary Information. The slopes of the regression plots varied from 0.80 with GISS-E2-1-H to 0.96 with UKESM1-0-LL showing that the compensation points determined with the MCMv3.3.1 overestimated those from the other mechanisms by between 4 – 20 % on average. An inter-mechanism uncertainty range was estimated at each of the 90 background locations, based on the maximum and minimum values over the eight chemical mechanisms. On this basis, the inter-mechanism range was about 0.17 ± 0.12 when expressed as a fraction of the average.

Closer inspection of the regression slopes versus MCMv3.3.1 in Figure S.1, showed that five mechanisms: BCC-GEOS-CHEMv1.0; CESM2-WACCM; GFDL-ESM4; MRI-ESM2-0 and

STOCHEM-CRI, gave values of slopes in a narrow range from 0.89 to 0.91. The slope value for GISS-E2-1-H at 0.80 was well outside of this range. OAT sensitivity experiments were performed to understand the possible influence of the four minor differences in the representation of C_1 chemistry in GISS-E2-1-H as revealed in Table S.1. Replacing the rate coefficient for the OH + MEPX reaction with that from other earth system models, moved the slope versus MCMv3.3.1 from 0.80 to 0.89, that is well within the range of the other models.

In an analogous manner, the slope versus MCMv3.3.1 for UKESM1-0-LL in Figure 1, with a value of 0.964, was significantly higher than that for some other mechanisms. OAT sensitivity analyses were performed to understand the importance of the twelve differences found in Table S.1 between the C_1 chemistry in UKESM1-0-LL, compared with that in some other earth system models. Removing all these differences caused the slope versus MCMv3.3.1 in Figure S.1 to move from 0.964 to 0.895, well within the range of the other earth system models. Of the many differences removed, as in section 2.4 above, the most important differences were with the representation of the OH + CH_3OOH reaction and its two reaction pathways.

On this basis, we have been able to show how differences in the two major compilations of evaluated chemical kinetic data: JPL (Burkholder et al., 2015) and IUPAC (Ammann et al., 2013), for the OH + CH_3OOH and CH_3O_2 + HO_2 reactions have led to discernible differences appearing in the NO_x compensation points estimated with the different chemical mechanisms in the pre-industrial atmosphere.

To construct an estimate of the likely uncertainty in the NO_x compensation points, a Monte Carlo uncertainty analysis was performed as described above, using the CESM2-WACCM model mechanism. Here, uncertainties in the fifteen thermal rate coefficients in the C_1 chemistry were taken from the JPL (Burkholder et al., 2015) data compilation and those for the three photochemical rate coefficients from our previous Monte Carlo studies (Derwent et al., 2018). The averages, standard deviations and ranges expressed as a fraction of the average NO_x compensation points were calculated for each of the 90 background locations over the 1000 constrained box model experiments. On average, over the 90 background locations, the range of the Monte Carlo replicates, expressed as a fraction of the average, was 0.50 ± 0.12 (where the confidence interval shown is 2 – σ). Figure 1 presents a scatter

plot of the NO_x compensation points determined for each background location versus the background O_3 mixing ratio for that location. Scatter plots are provided for each model chemical mechanism and the close correlation between the mechanisms is clearly apparent. Also shown are the error bars for CESM2-WACCM calculated in the Monte Carlo uncertainty analysis of the C_1 chemical kinetic input data uncertainties. On the basis of this figure, the inter-mechanism ranges of 0.17 ± 0.12 are close to a factor of three smaller than the intra-mechanism ranges of 0.50 ± 0.12, in the NO_x compensation points at each location as evaluated by the Monte Carlo uncertainty analysis of the CESM2-WACCM C_1 chemical kinetic input uncertainties.

4. Impacts of organic compounds on OH radicals

In this section, the impacts of four organic compounds: CH_4, C_2H_6, CH_3COCH_3 and C_3H_8 on OH radicals were investigated using the constrained box model. The experimental details are presented in the Supplementary Information. Small additions of all four compounds led to small depletions in the time-averaged hydroxyl radical number densities ($\underline{OH}$) in all 90 background locations and with all chemical mechanisms. The hydroxyl responses ($\Delta\ \underline{OH}$) declined linearly with the increases in the rates of oxidation of the organic compound (Δ R). Scatter plots of $\Delta\ \underline{OH}$ versus Δ R covering all background locations produced a family of straight lines for each chemical mechanism and each organic compound, as shown in Figures S.2 – S.4 for CH_4, C_2H_6 and C_3H_8 as examples. The variations in the slopes of these scatter plots between the different chemical mechanisms and organic compounds reflected the divergences in the representation of C_1 – C_3 chemistry and its ability to recycle OH back to HO_2 through the different organic peroxy radicals.

Each organic compound addition experiment at a given background location generated a value for the hydroxyl reactivity ratio (HRR), ($HRR = \Delta\ \underline{OH}\ /\ \Delta$ R) for a given chemical mechanism. The Supplementary Information describes how a total of 90 (background locations) x 8 (chemical mechanisms) x 4 (organic compounds) HRRs were generated using the constrained box model. Figure 2, as an example, presents a scatter plot of the HRR_{CH4} values versus the background temperatures found at each location with the different chemical mechanisms. The close relationship between the HRRs and background temperatures seen in Figure 2 reflects the important influence of temperature on the relationship between the oxidation rates of the organic compounds and OH depletion.

HRR_{CH4} values vary from (-12 to -30) x 10^6 molecule cm^{-3} per ppb hr^{-1}, that is by a factor of 2.5, with decreasing temperature over a narrow range of ~ 25 K, see Figure 2. This temperature dependence follows from the steep temperature dependences found in the rate coefficients for the OH + CH_4 and HO_2 + O_3 chemical reactions. Inter-mechanism ranges were estimated at each background location and expressed as a fraction of the average. These fractional ranges were averaged over all the background locations and are presented in Table 4. Fractional inter-mechanism ranges increased from 0.18 ± 0.05 for HRR_{CH4}, through ethane and propane, to 0.63 ± 0.2 for $HRR_{CH3COCH3}$.

Also shown in Figure 2 are the results from the Monte Carlo uncertainty analysis of CESM2-WACCM, employing C_1 rate coefficient uncertainties taken from the JPL chemical kinetic data evaluation (Burkholder et al., 2015). The error bars show the extent of the maxima and minima found in 1000 Monte Carlo replicates at the 90 background locations with the CESM2-WACCM model mechanism. More negative values of HRR_{CH4} have wider error bars than less negative values. Fractional intra-mechanism ranges in HRR_{CH4} averaged out at 0.53 ± 0.06 when expressed as a fraction of the mean value, see Table 4. Intra-mechanism ranges in HRR_{CH4} are close to a factor of three wider than inter-mechanism ranges (0.18 ± 0.05). Fractional intra-mechanism ranges in HRR_{C2H6} and HRR_{C3H8} were close to a factor of two wider than fractional inter-mechanism ranges, and a factor of 2.6 wider with $HRR_{CH3COCH3}$, see Table 4.

5. Impacts of organic compounds on tropospheric ozone

In this section, the impacts of four organic compounds: CH_4, C_2H_6, CH_3COCH_3 and C_3H_8 on the net production rates of tropospheric O_3 were investigated using the constrained box model. The experimental details are presented in the Supplementary Information. Small additions of all four compounds led to small increases in the time-averaged net O_3 production rates in all 90 background locations and with all chemical mechanisms. In response to the addition of the four organic compounds, the flux through the organic peroxy (RO_2) + NO reactions increased and acted as an increased O_3 source. This was partially offset by a decrease in the flux through the HO_2 + NO reaction because of the depletion in OH and HO2 brought about by the oxidation of the organic compound. However, the decrease in OH and HO_2 also caused decreases in the fluxes through the O_3 sink reactions: OH + O_3 and HO_2 + O_3. Overall, net O_3 production (source – sink) increased in

response to the addition of the organic compounds at all 90 locations and with all chemical mechanisms.

The responses in the net rate of O_3 production, Δ net_{O3} increased with the rate of oxidation of the organic compound Δ R as shown by the scatter plots in Figures S.5 – S.8. OAT sensitivity tests confirmed that all of the differences in the scatter plots between the mechanisms could be accounted for by differences in the reaction rate coefficients and product yields for the RO_2 + HO_2 and OH + ROOH reactions in Tables S.1 – S.3 in the Supplementary Information. The results of each organic compound addition experiment were used to define an O_3 formation potential (OFP), such that OFP = Δ net_{O3} / Δ R, at each of the 90 background locations, with each chemical mechanism and for each organic compound. OFPs were found to increase systematically with increasing background NO_x as shown in Figures 3 – 6. Also shown in each figure are a set of error bars which reflect the range between the maximum and minimum OFPs found at that background location in the Monte Carlo uncertainty analysis of the rate coefficient uncertainties in the C_1 – C_3 chemistry with the CESM2-WACCM model chemical mechanism. The results presented in Figures 3 – 6 are summarised in Table 4.

OFPs were highest for CH_3COCH_3 and lowest for C_3H_8, with $OFP_{CH3COCH3}$ > OFP_{C2H6} > OFP_{CH4} > OFP_{C3H8}. Fractional inter-mechanism ranges were smallest for C_2H_6 and largest for CH_3COCH_3 whilst fractional intra-mechanism ranges were smallest for CH_4 and largest for C_3H_8. Intra-mechanism ranges were nearly seven times wider than inter-mechanism ranges for C_2H_6 because mechanism developers had converged on similar descriptions of C_2 chemistry, see Table S.2, despite there being huge uncertainties in the laboratory determinations of the $C_2H_5O_2$ + HO_2 and OH + C_2H_5OOH rate coefficients and products yields. Intra-mechanism ranges were 1.5 times wider for CH_4, twice as wide for CH_3COCH_3 and nearly three times wider for C_3H_8.

6. Discussion and conclusions

Emissions of organic compounds exert two main impacts on the chemistry of the present day and pre-industrial troposphere: depletion of the OH radical steady state and stimulation of photochemical O_3 formation. Depletion of the OH radical steady state is the driving force behind the CH_4 adjustment time (Prather, 2007) and the indirect radiative forcing caused by

organic compounds (Collins et al., 2002). OH steady state depletion leads to the decreased efficiency of global CH_4 removal and hence increased global burdens of CH_4, the second most important contributor to man-made greenhouse gas radiative forcing after CO_2. Increased photochemical O_3 formation from the oxidation of organic compounds also leads to indirect radiative forcing because tropospheric O_3 is the third most important contributor to man-made greenhouse gas radiative forcing after CO_2 and CH_4. These two impacts of organic compounds have been examined using a constrained box model and form the subject of this earth system model intercomparison.

Addition of four organic compounds: CH_4, C_2H_6, CH_3COCH_3 and C_3H_8, into the constrained box model representing the pre-industrial troposphere, resulted in depletion of OH across all 90 background locations and with all chemical mechanisms. A hydroxyl radical reactivity index (HRR) has been defined for each organic species from the ratio of the depletion in OH to the rate of oxidation of the organic compound at each location and with each chemical mechanism. Table 4 presents a comparison of the mean HRRs for each chemical mechanism. HRRs were stronger (greater depletion) for the alkanes and weaker for CH_3COCH_3. Inter-mechanism uncertainties in the HRRs were quantified in Table 4 using inter-mechanism ranges expressed as a fraction of the inter-mechanism average. On this basis, uncertainties were largest (0.63 ± 0.2) for CH_3COCH_3 and least for CH_4 (0.18 ± 0.05).

One-at-a-time (OAT) sensitivity studies confirmed that two sets of reactions accounted for the divergences noted in Table 4 in the HRRs between the different chemical mechanisms, namely, OH + ROOH (in particular, OH + CH_3OOH) and RO_2 + HO_2 (in particular, CH_3O_2 + HO_2). The divergences found in the HRRs in Table 4 stem directly from the choices made by the mechanism developers for chemical kinetic data for C_1 – C_3 chemistry. The evaluated chemical kinetic data evaluations offer little coverage of C_3 chemistry and hence differences in its representation in chemical mechanisms are unavoidable for CH_3COCH_3 and C_3H_8. This situation inevitably leads to the increased ranges in the HRRs presented in Table 4.

The inter-mechanism ranges in Table 4 are driven by the choices made by mechanism developers for some key rate coefficients and product yields and these ultimately lead back to the differences in the evaluations between the two major chemical kinetic data compilations, JPL (Burkholder et al., 2015) and IUPAC (Ammann et al., 2013). However, both evaluations point to the large uncertainties present in the laboratory determinations of rate

coefficients and product channel branching ratios for some key RO_2 + HO_2 and OH + ROOH reactions. Indeed, IUPAC (Amman et al., 2013) comment that the reported values for HO_2 + $C_2H_5O_2$ at 298 K show a level of disagreement covering almost a factor of three. It is these uncertainties that drive the intra-mechanism ranges found with the Monte Carlo uncertainty analysis carried out with the CESM2-WACCM model chemical mechanism. Generally speaking, intra-mechanism ranges in the HRRs in Table 4 were much larger than the inter-mechanism ranges. Therefore, our conclusions concerning the uncertainties in HRRs focus directly on the inadequacy of the literature chemical kinetic database rather than on the apparent divergences between the IUPAC (Amman et al., 2013) and JPL (Burkholder et al., 2015) chemical kinetic data evaluations. It is not surprising that these two evaluations diverge, bearing in mind the large uncertainties that exist surrounding RO_2 + HO_2 and OH + ROOH rate coefficients and product channel branching ratios. Inter-model ranges are therefore likely to provide a gross underestimation of the real uncertainties in earth system model predictions of the time evolution in tropospheric CH_4 levels from pre-industrial times through to the present day.

Earth system models also have an important climate policy support role through their ability to describe the growth in tropospheric O_3 levels since pre-industrial times, since this allows the direct quantification of the contribution to radiative forcing from tropospheric O_3. A major determinant of this growth is the rise in global NO_x emissions since this controls the spatial distribution of O_3 source regions at any point in time between pre-industrial times and the present day. The point at which tropospheric chemistry turns from being an O_3 sink to an O_3 source with increasing NO_x levels is termed the NO_x compensation point and these have been determined for each chemical mechanism and each background location with the constrained box model for pre-industrial conditions. Compensation points increased from about 9 ppt to close to 70 ppt as background O_3 levels increased from 7 ppb to 21 ppb. The inter-mechanism uncertainty range averaged 0.17 ± 0.12 and was largely driven by the choice of rate coefficients and product yields for the OH + CH_3OOH and HO_2 + CH_3O_2 reactions. The intra-mechanism uncertainty range from the Monte Carlo uncertainty analysis of the CESM2-WACCM model chemistry was found to be 0.50 ± 0.12. This is close to a factor of three wider than the inter-mechanism range.

Compensation points quantify the NO_x conditions where O_3 sources and sinks balance but O_3 productivities quantify the intensity of net O_3 production in a given source region. Table 4 presents the ozone formation potentials (OFPs) for CH_4, C_2H_6, CH_3COCH_3 and C_3H_8 as determined from the scatter plots in Figures 3 – 6. OFPs are largest for C_2H_6 and CH_3COCH_3 and smallest for CH_4 and C_3H_8. Inter-mechanism ranges in the OFPs in Table 4 were highest for CH_3COCH_3 and C_3H_8 because of the increased complexity of C_3 chemistry and were least for C_2H_6. In all cases, the intra-mechanism ranges from the Monte Carlo uncertainty analyses were significantly wider than the inter-mechanism ranges. This was particularly noticeable for C_2H_6 where the intra-mechanism range was more than six times wider than the inter-mechanism range. Similarly, a factor of three was apparent for C_3H_8. The inter-mechanism ranges were therefore a poor guide to the real uncertainties in OFPs because there was little divergence in the chosen values of rate coefficients for the $RO_2 + HO_2$ and OH + ROOH reactions, despite the huge uncertainties in these rate coefficients. This real level of uncertainty only became apparent in the Monte Carlo uncertainty analyses.

Solazzo and Galmarini (2015) offer a careful consideration of ensembles of opportunity, which is evidently the situation here, where six earth system models from the CMIP6 study have been intercompared alongside two other chemical mechanisms. Solazzo and Galmarini (2015) point out that simply averaging model simulations may provide an illusory estimate of model uncertainty. Inter-mechanism ranges found here for HRRs and OFPs are all significantly smaller than real uncertainty ranges found from Monte Carlo uncertainty analyses. The results found here for the OFP for ethane are a classic example of one of the pitfalls of ensembles of opportunity identified by Solazzo and Galmarini (2015). The processes of standardisation and coordination have led model developers to use common rate coefficients and product channel branching ratios for $RO_2 + HO_2$ and OH + ROOH reactions and so have hid real uncertainties. Inter-mechanism ranges, therefore, are unlikely to reflect true uncertainties.

Further work will be required to understand whether the uncertainties found here persist into earth system model predictions of the growth in CH_4 and tropospheric O_3 levels between pre-industrial times and the present day. It is tempting to offer an explanation for the differences seen in pre-industrial O_3 in the six ESMs that took part in CMIP6 (Eyring et al., 2016) in terms of the differences found here. GISS-E2-1-H, for example, exhibited the

lowest average NO_x compensation point and the lowest pre-industrial annual mean at Cape Grim, Tasmania whilst UKESM1-0-LL exhibited the highest on both counts. In which case, it is possible that inter-mechanism ranges in CMIP6 underestimate real uncertainties in pre-industrial O_3 predictions by a wide margin. Real uncertainties are unlikely to be revealed by multi-model comparisons because model developers use common assumptions when input data are highly uncertain as shown here with the $RO_2 + HO_2$ and OH + ROOH rate coefficients and product channel branching ratios. Further definitive laboratory studies are required for more accurately defining the reaction rates and product yields of the reactions of the simple peroxy radicals, between themselves and with HO_2 and of the fates and behaviour of the simple hydroperoxides. Such future studies should aim to reduce the uncertainties in key reaction rate coefficients and determine whether they contribute significantly to the uncertainties in earth system model projections since pre-industrial times of CH_4 and O_3 and hence to the radiative forcing of climate change.

Acknowledgements

RGD wishes to thank the Earth System Modelling teams for providing access to their chemical mechanisms. MD was partly supported by JSPS KAKENHI grant no. JP19K12312. DES and MAHK thank NERC (Grant code-NE/K004905/1), Bristol ChemLabS and Primary Science Teaching Trust under whose auspices various aspects of this work using STOCHEM-CRI were supported. DS thanks NASA GISS and MAP for funding. Help from Louisa Emmons, John Orlando and Geoff Tyndall for providing and developing the MOZART family of chemical mechanisms is gratefully acknowledged. RGD acknowledges help from Michael Jenkin with the implementation of the MCMv3.3.1 and CRIv2.2 chemical mechanisms and from Mat Evans with the implementation of GEOS-CHEM. ATA would like to thank the Met Office and NCAS for funding for the development of the UKCA model through the auspices of the Joint Weather and Climate Research Programme. SET and KT acknowledge NASA MAP for funding. GISS-E2-1-H resources supporting this work were provided by the NASA High-End Computing (HEC) Programme through the Center for Climate Simulation (NCSS) at Goddard Space Flight Center.

References

Ammann, M., Cox, R.A., Jenkin, M.E., Melhouki, A., Rossi, M.J., Troe, J., Wallington, T.J., 2013. Evaluated kinetic and photochemical data for atmospheric chemistry: Volume VI – heterogeneous reactions with liquid substrates. Atmospheric Chemistry and Physics 13, 8045-8228.

Archibald, A.T., O'Connor, F.M., Abrahm, N.L., Archer-Nicholls, S., Chipperfield, M.P., Dalvi, M., Folberth, G.A., Dennison, F., Dhomse, S.S., Griffiths, P.T., Hardacre, C., Hewitt, A. J., Hill, S.R., Johnson, C.E., Keeble, J., Kohler, M.O., Morgenstern, O., Mulcahy, J.P., Ordonez, C., Pope, R.J., Rumbold, S.T., Russo, M.R., Savage, N.H., Sellar, A., Stringer, M., Turnock, S.T., Wild, O., Zeng, G., 2020. Description and evaluation of the UKCA stratosphere-troposphere chemistry scheme (StratTrop vv 1.0) implemented in UKESM1. Geoscientific Model Development 13, 1223-1266.

Archibald, A.T., Neu, J.L., Elshorbany, Y., Cooper, O.R., Young, P.J., Akiyoshi< H., Cox, R.A., Coyle, M., Derwent, R.G., Deushi, M., Finco, A., Frost, G.J., Galbally, I.E., Gerosa, G., Granier, C., Griffiths, P.T., Hossani, R., Hu, L., Jockel, P., Josse, B., Lin, M.Y., Mertens, M., Morgenstern, O., Naja, M., Naik, V., Saiz-Lopez, A., Saxena, P., Shin, Y.M., Shaahid, I., Shallcross, D.E., Tilnes, S., Wallington, T.J., TRickel, T., Wang, T., Worden, H.M., Zeng, G., 2020. Tropospheric Ozone Assessment Report: Critical review of changes in the tropospheric ozone burden and budget from 1960 – 2100. Elementa: Science of the Anthropocene.

Burkholder, J.B., Sander, S.P., Abbatt, J., Barker, J.R., Huie, R.E., Kolb, C.E., Kurylo, M.J., Orkin, V.L., Wilmouth, D.M., Wine, P.H., 2015. Chemical kinetics and photochemical data for use in atmospheric studies. Evaluation No. 18. JPL Publication 15-10. Jet Propulsion Laboratory, Pasadena. http://jpleval.jpl.nasa.gov.

Calvert, J.G., Derwent, R.G., Orlando, J.J., Tyndall, G.S., Wallington, T.J., 2008. Mechanisms of atmospheric oxidation of the alkanes. Oxford University Press, Oxford, UK.

Collins, W.J., Derwent, R.G., Johnson, C.E., Stevenson, D.S., 2002. The oxidation of organic compounds in the troposphere and their global warming potentials. Climatic Change 52, 453-47.

Crutzen, P.J., 1974. Photochemical reactions initiated by and influencing ozone in the polluted troposphere. Tellus 26, 47-57.

Curtis, A.R., Sweetenham, W.P., 1987. FACSIMILE release H user's manual. AERE Report R11771, H.M. Stationery Office, London.

Derwent, R., 2017. Intercomparison of chemical mechanisms for air quality policy formulation and assessment under North American conditions. Journal of the Air and Waste Management Association 67, 789-796.

Derwent, R.G., 2020. Representing organic compound oxidation in chemical mechanisms for policy-relevant air quality models under background troposphere conditions. Atmosphere 11, 171, doi:10.3390/atmos11020171.

Derwent, R.G., Witham, C.S., Utembe, S.R., Jenkin, M.E., Passant, N.R., 2010. Ozone in Central England: the impact of 20 years of precursor emission controls in Europe. Environmental Science and Policy 13, 195-204.

Derwent, R.G., Utembe, S.R., Jenkin, M.E., Shallcross, D.E., 2015. Tropospheric ozone production regions and the intercontinental origins of surface ozone. Atmospheric Environment 112, 216-224.

Dunne, J.P., Horowitz, L.W., Adcroft, A.J., Ginoux, P., Held, I.M., John, J.G., Krasting, J.P., Malyshev, S., Naik, V., Paulot, F., Shevliakova, E., Stock, C.A., Zadeh, N., Balaji, V., Blanton, C., Dunne, K.A., Dupuis, C., Durachta, J., Dussin, R., Gauthier, P.P.G., Griffies, S.,M., Guo, H., Hallberg, R.W., Harrison, M., He, J., Hurlin, W., McHugh, C., Menzel, R., Milly, P.C.D., Nikonov, S., Paynter, D.J., Ploshay, J., Radhakrishnan, A., Rand, K., Reichl, B.G., Robinson, T., Schwarzkopf, M.D., Sentman, L.A., Underwood, S., Vahlenkamp, H., Winton, M., Wittenberg, A.T., Wyman, B., Zeng, Y., Zhao. M., 2020. The GFDL Earth System Model version 4.1 (GFDL-ESM4.1): Model description and simulation characteristics, submitted to Journal of Advances in Modeling Earth Systems. 2019MS002008.

Emmerson, K.M., Evans, M.J., 2009. Comparison of tropospheric gas-phase chemistry schemes for use within global models. Atmospheric Chemistry and Physics 9, 1831-1845.

Emmons, L.K., Walters, S., Hess, P.G., Lamarque, J.-F., Pfister, G.G., Fillmore, D., Granier, C., Guenther, A., Kinnison, D., Laepple, T., Orlando, J., Tie, X., Tyndall, G., Wiedinmyer, C., Baughcum, S.L., Kloster, S., 2010. Description and evaluation of the Model for Ozone and Related chemical Tracers, vesion 4 (MOZART-4). Geoscientific Model Development 3, 43-67.

Emmons, L.K., Schwantes, R.H., Orlando, J.J., Tyndall, G., Kinnison, D., Lamarque, J.-F., Marsh, D., Mills, M.J., Tilmes, S., Bardeen C., Buchholz, R.R., Conley, A., Gettelman, A., Garcia, R., Simpson, I., Blake, D.R., Meinardi, S., Petron, G., 2020. The chemistry mechanism in the Community Earth System Model Version 2 (CESM2). Journal of Advances in Modeling Earth Systems 12, e2019MS001882. https//doi.org/10.1029/2019MS001882.

ENVIRON, 2015. Appendix C, CAMx User's Guide Version 6.2, Environ International Corporation, Novato, California, March 2015.

Etheridge, D.M., Pearman, G.I., Fraser, P.J., 1992. Changes in tropospheric methane between 1841 and 1978 from a high accumulation-rate Antarctic ice core. Tellus B 44, 282-294.

Eyring, V., Bony, S., Meehl, G.A., Senior, C.A., Stevens, B., Stouffer, Taylor, K.E., 2016. Overview of the Coupled Model Intercomparison Project Phase 6 (CMIP6) experimental design and organization. Geoscientific Model Development 9, 1937-1958.

Gettelman, A., Mills, M. J., Kinnison, D. E., Garcia, R. R., Smith, A. K., Marsh, D. R., et al., 2019. The whole atmosphere community climate model version 6 (WACCM6). Journal of Geophysical Research Atmospheres, https://doi.org/10.1029/ 2019JD030943.

Hall, S.R., Ullmann, K.R., Prather, M.J., Flynn, C.M., Murray, L.T., Fiore, A.M., Correa, G., Stode, S.A., Steenrod, S.D., Lamarque, J.-F., Guth, J., Josse, B., Flemming, J., Huijnen, V., Abraham, N.L., Archibald, A.T., 2018. Cloud impacts on photochemistry: building a climatology of photolysis rates from the Atmospheric Tomography mission. Atmospheric chemistry and Physics 18, 16809-16828.

IPCC, 1990. Climate change: The IPCC scientific assessment (1990). Cambridge University Press, Cambridge, UK.

IPCC, 1996. Climate change 1995: The science of climate change. Cambridge University Press, Cambridge, UK.

IPCC, 2001. Climate change 2001: The scientific basis. Cambridge University Press, Cambridge, UK.

IPCC, 2013. Climate change 2013: The physical science basis. Cambridge University Press, Cambridge, UK.

Jenkin, M.E., Khan, M.A.H., Shallcross, D.E., Bergstrom, R., Simpson, D., Murphy, K.L.C., Rickard, A.R., 2019. Atmospheric Environment 212, 172-182.

Jenkin, M.E., Young, J.C., Rickard, A.R., 2015. The MCM v3.3.1 degradation scheme for isoprene. Atmospheric Chemistry and Physics 15, 11433-11459.

Kelley, M., Schmidt, G.A., Nazarenko, L., Bauer, S.E., Ruedy, R., Russell, G.L., Ackerman, A.S., Aleinov, I., Bauer, M., Bleck, R., + 36 co-authors, 2020. GISS-E2.1: Configurations and climatology. Journal of Advances in Modeling Earth Systems, doi:10.1029/2019MS002025.

Khalil, M.A.K., Rasmussen, R.A. 1988. Nitrous oxide: Trends and global mass balance over the last 3000 years. Annals of Glaciology 10, 73-79.

Khan, M.A.H., Miles, B., Jenkin, M.E., Derwent, R.G., Percival, C.J., Shallcross, D.E., 2020. Investigating the impacts of non-acyl peroxy nitrates on the global composition of the troposphere using a 3-D chemical transport model, STOCHEM-CRI. American Chemical Society Earth and Space Chemistry 4, 1201-1212.

Khan, M.A.H., Schlich, B.-L., Jenkin, M.E., Cooke, M.C., Derwent, R.G., Neu, J.L., Percival, C.J., Shallcross, D.E., 2021. Changes to simulated global atmospheric composition resulting from recent revisions to isoprene oxidation chemistry. Atmospheric Environment 244, 117914.

Levy, H., 1972. Photochemistry of the lower troposphere. Planetary and Space Science 20, 919-935.

Monks, P.S., Archibald, A.T., Colette, A., Cooper, O., Coyle, M., Derwent, R., Fowler, D., Granier, C., Law, K.S., Mills, G.E., Stevenson, D.S., Tarasova, O., Thouret, V., von Schneidemesser, E., Sommariva, R., Wild, O., Williams, M.L., 2015. Tropospheric ozone and its precursors from the urban to the global scale from air quality to short-lived climate forcer. Atmospheric Chemistry and Physics 15, 8889-8973.

Naik, V., et al., 2013. Preindustrial to present-day changes in tropospheric hydroxyl radical and methane lifetime from the Atmospheric Chemistry and Climate Model Intercomparison Project (ACCMIP). Atmospheric Chemistry and Physics 13, 5277-5298.

Newsome, B., Evans, M., 2017. Impact of uncertainties in inorganic chemical rate constants on tropospheric composition and ozone radiative forcing. Atmospheric Chemistry and Physics 17, 14333-14352.

Parrish, D.D., Derwent, R.G., Turnock, S.T., O'Connor, F.M., Staehelin, J., Bauer, S.E., Deushi, M., Oshima, N., Tsigaridis, K., Wu, T., Zhang, J., 2020. Anthropogenic reversal of the natural ozone gradient between northern and southern mid-latitudes. Submitted to Proceedings of the National Academy of Sciences.

Prather, M.J., 2007. Lifetimes and time scales in atmospheric chemistry. Philosophical Transactions of the Royal Society A 365, 1705-1726.

Raynaud, D., Barnola, 1985. An Antarctic ice core reveals atmospheric CO_2 variations over the past few centuries. Nature 315, 309-311.

Revell, L.E., Stenke, A., Tummon, F., Feinberg, A., Rozanov, E., Peter, T., Abraham, N.L., Akiyoshi, H., Archibald, A.T., Butchart, N., Deushi, M., Jockel, P., Kinnison, D., Michou, M., Morgenstern, O., O'Connor, F.M., Oman, L.D., Pitari, G., Plummer, D.A., Schofield, R., Stone, K., Tilmes, S., Visioni, D., Yamahita, Y., Zeng, G., 2018. Tropospheric ozone in CCMI models and Gaussian process emulation to understand biases in the SOCOLv3 chemistry-climate model. Atmospheric Chemistry and Physics 18, 16155-16172.

Sellar, A. A., Jones, C. G., Mulcahy, J., Tang, Y., Yool, A., Wiltshire, A., O'Connor, F. M., Stringer, M., Hill, R., Palmieri, J., Woodward, S., Mora, L., Kuhlbrodt, T., Rumbold, S., Kelley, D. I., Ellis, R., Johnson, C. E., Walton, J., Abraham, N. L., Andrews, M. B., Andrews, T., Archibald, A. T., Berthou, S., Burke, E., Blockley, E., Carslaw, K., Dalvi, M., Edwards, J., Folberth, G. A., Gedney, N., Griffiths, P. T., Harper, A. B., Hendry, M. A., Hewitt, A. J., Johnson, B., Jones, A., Jones, C. D., Keeble, J., Liddicoat, S., Morgenstern, O., Parker, R. J., Predoi, V., Robertson, E., Siahaan, A., Smith, R. S., Swaminathan, R., Woodhouse, M. T., Zeng, G., Zerroukat, M., 2019. UKESM1: Description and evaluation of the UK Earth System Model, J. Adv. Model. Earth Syst., 2019MS001739, doi:10.1029/2019MS001739.

Solazzo, E., Galmarini, S., 2015. A science-based use of ensembles of opportunities for assessment and scenario studies. Atmospheric Chemistry and Physics 15, 2535-2544.

Tilmes, S., Hodzic, A., Emmons, L. K., Mills, M. J., Gettelman, A., Kinnison, D. E., Park, M., Lamarque, J. -F., Vitt, F., Shrivastava, M., Campuzano Jost, P., Jimenez, J., Liu, X., 2019. Climate forcing and trends of organic aerosols in the Community Earth System Model (CESM2). Journal of Advances in Modeling Earth Systems, 2019MS001827, doi:10.1029/2019MS001827.

Utembe, S.R., et al., 2010. Using a reduced Common Representative Intermediates (CRIv2-R5) mechanism to simulate tropospheric ozone in a 3-D Lagrangian chemistry transport model. Atmospheric Environment 44, 1609-1622.

Wang, Y., Jacob, D.J., 1998. Anthropogenic forcing on tropospheric ozone and OH since preindustrial times. Journal of Geophysical Research 103, 31,123-31,136.

Wild, O., Voulgarakis, A., O'Connor, F., Lamarque, J.-F., Ryan, E.M., Lee, L., 2020. Global sensitivity analysis of chemistry-climate model budgets of tropospheric ozone and OH: Exploring model diversity. Atmospheric Chemistry and Physics 20, 4047-4058.

Wu, T., Lu, Y., Fang, Y., Xin, X., Li, L., Li, W., Jie, W., Zhang, J., Liu, Y., Zhang, L., Zhang, F., Zhang, Y., Wu, F., Li, J., Chu, M., Wang, Z., Shi, X., Liu, X., Wei, M., Huang, A., Zhang, Y., Liu, X., 2019. The Beijing Climate Center Climate System Model (BCC-CSM): the main progress from CMIP5 to CMIP6. Geoscientific Model Development 12, 1573–1600. doi:10.5194/gmd-12-1573-2019, 2019. 552

Wu, T., Zhang, F., Zhang, J., Jie, W., Zhang, Y., Wu, F., Li, L., Yan, J., Liu, X., Lu, X., Tan, H., Zhang, L., Wang, J., Hu, A., 2020. Beijing Climate Center Earth System Model version 1 (BCC-ESM1): Model Description and Evaluation of Aerosol Simulations. Geoscientific Model Development 13, 977–1005. doi:10.5194/gmd-13-977-2020.

Young, P.J. et al., 2013. Pre-industrial to end 21st century projections of tropospheric ozone from the Atmospheric Chemistry and Climate Model Intercomparison Project (ACCMIP). Atmospheric Chemistry and Physics 13, 2063-2090.

Young, P.J., and 29 co-authors, 2018. Tropospheric ozone assessment report: Assessment of global-scale model performance for global and regional ozone distributions, variability and trends. Elementa Science of the Anthropocene 6:10. Doi://https/doi.org/10.10.1525/elementa.265.

Yukimoto, S., Kawai, H., Koshiro, T., Oshima, N., Yoshida, K., Urakawa, S., Tsujino, H., Deushi, M., Tanaka, T., Hosaka, M., Yabu, S., Yoshimura, H., Shindo, E., Mizuta, R., Obata, A., Adachi, Y., Ishii, M., 2019. The Meteorological Research Institute Earth System Model Version 2.0, MRI-ESM2.0: Description and basic evaluation of the physical component. Journal of the Meteorological Society of Japan 97, 931-965.

Table 1. The earth system and other global models, their chemical mechanisms employed in this intercomparison, together with their supporting references.

Model or chemical mechanism	References
BCC-GEOS-CHEMv1.0	Wu et al., 2019a, b Mao et al. 2010, 2013 Parrella et al., 2012 Emmerson and Evans, 2009*
CESM2-WACCM	Emmons et al., 2020* Gettelman et al., 2019 Tilmes et al., 2019
GFDL-ESM4	Dunne et al., 2019 Horowitz et al., 2019*
GISS-E2-1-H	Kelley et al., 2020 Shindell et al., 2001*
MRI-ESM2-0	Deushi and Shibata, 2011* Yukimoto et al., 2019
UKESM-1-0-LL	Sellar et al., 2019 Archibald et al., 2020*
MCMv3.3.1	Jenkin et al., 2015*
STOCHEM-CRI	Utembe et al., 2010 Jenkin et al., 2019 Khan et al., 2021* www.cri.york.ac.uk

Notes:

*, denotes the reference supporting the chemical mechanism.

Table 2. Pre-industrial background mixing ratios for key species employed in the constrained box model. The second column gives the simplified conditions for a single location for use in the test and evaluation phase. The third column gives the range of assumed background environmental conditions which were derived from STOCHEM-CRI simulations at ninety global locations.

Species	Simplified test conditions	Pre-industrial mixing ratio
CH_4	700 ppb	705 – 843 ppb
O_3	15 ppb	7.4 – 20.6 ppb
CO	52 ppb	47 – 117 ppb
H_2	499 ppb	499 ppb
NO	3 ppt	0.15 – 15.2 ppt
NO_2	16 ppt	3.3 – 122 ppt
HNO_3		0.9 – 126 ppt
PAN		0.7 – 80 ppt
MPAN		0 – 3.8 ppt
H_2O_2		0.02 – 1.3 ppb
CH_3OOH		0.003 – 0.9 ppb
HCHO		0.02 – 1.46 ppb
CH_3CHO		1.6 – 120 ppt
C_2H_6		88 – 691 ppt
C_3H_8		6 – 332 ppt
nC_4H_{10}		0.9 – 488 ppt
C_2H_4		0 – 1.9 ppb
C_3H_6		0 – 0.88 ppb
C_2H_5CHO		0 – 1.5 ppt
CH_3COCH_3		0.17 – 1.5 ppb
CH_3OH		142 – 844 ppt
C_5H_8		0 – 7.6 ppb
Atmospheric number density, molecule cm^{-3}	$2.3603.10^{19}$	$1.84 – 2.516.10^{19}$
Water vapour number density, molecule cm^{-3}	$5.6907.10^{17}$	$1.277 – 6.395.10^{17}$
Temperature, K	295.7	277.7 – 303.8

Table 3. Time-averaged photochemical ozone production rates (P_{O3}) and number densities of OH (OH) and HO_2 (HO_2) estimated with the constrained box model with each chemical mechanism under the simplified test conditions in the pre-industrial atmosphere.

Mechanism	P_{O3}, ppb hr^{-1}	OH , 10^6 cm^{-3}	HO_2 , 10^8 cm^{-3}
BCC-GEOS-CHEMv1.0	0.0409	2.024	1.477
CESM2-WACCM	0.0410	2.023	1.474
GFDL-ESM4	0.0409	2.024	1.477
GISS-E2-1-H	0.0422	1.915	1.402
MRI-ESM2.0	0.0406	2.045	1.504
UKESM1-0-LL	0.0399	2.102	1.542
STOCHEM-CRI	0.0409	2.027	1.481
MCMv3.3.1	0.0407	2.043	1.493
Fractional range	0.064	0.071	0.10

Notes:

The number of decimal places does not represent intrinsic accuracy but is merely to facilitate comparisons.

Fractional range = (maximum-minimum)/average

Table 4. Summary of the HRRs and OFPs estimated for each organic compound with each chemical mechanism, together with the estimated fractional inter-mechanism and with the intra-mechanism ranges from Monte Carlo uncertainty analyses.

Mechanism	methane	ethane	acetone	propane

HRR = Response in OH expressed as a ratio of the increment in the rate of organic compound oxidation in 10^6 ppb hr^{-1}

BCC-GEOS-CHEMv1.0	-20.8 ± 8	-21.1 ± 7	-10.8 ± 6	-18.7 ± 6
CESM2-WACCM	-20.9 ± 8	-20.4 ± 7	-9.8 ± 5	-22.5 ± 8
GFDL-ESM4	-20.9 ± 8	-20.6 ± 7	-10.1 ± 5	-22.6 ± 9
GISS-E2-1-H	-22.7 ± 8			
MRI-ESM2.0	-19.9 ± 7	-24.6 ± 9	-15.1 ± 6	-23.3 ± 9
UKESM1-0-LL	-18.9 ± 6	-24.9 ± 10	-16.7 ± 9	-18.3 ± 6
STOCHEM-CRI	-21.2 ± 8	-20.0 ± 7	-10.6 ± 7	-15.8 ± 5
MCMv3.3.1	-21.5 ± 8	-21.6 ± 8	-10.3 ± 6	-17.7 ± 5
Fractional Inter-mechanism range	0.18 ± 0.05	0.24 ± 0.05	0.63 ± 0.2	0.38 ± 0.16
Fractional Intra-mechanism range	0.53 ± 0.06	0.45 ± 0.09	1.65 ± 0.4	0.69 ± 0.07

OFP = Response in time-averaged rate of net ozone production expressed as a ratio of the increment in the rate of organic compound oxidation in ppb hr^{-1}

BCC-GEOS-CHEMv1.0	0.43 ± 0.2	0.64 ± 0.5	0.81 ± 0.8	0.50 ± 0.3
CESM2-WACCM	0.43 ± 0.2	0.62 ± 0.6	0.81 ± 0.9	0.43 ± 0.2
GFDL-ESM4	0.43 ± 0.2	0.61 ± 0.6	0.57 ± 0.7	0.43 ± 0.2
GISS-E2-1-H	0.48 ± 0.2			
MRI-ESM2.0	0.38 ± 0.2	0.64 ± 0.6	0.57 ± 0.7	0.44 ± 0.2
UKESM1-0-LL	0.35 ± 0.2	0.69 ± 0.3	0.58 ± 0.7	0.40 ± 0.3
STOCHEM-CRI	0.42 ± 0.2	0.70 ± 0.6	0.74 ± 0.7	0.39 ± 0.3
MCMv3.3.1	0.37 ± 0.2	0.70 ± 0.6	0.82 ± 0.8	0.33 ± 0.2
Fractional Inter-mechanism range	0.31 ± 0.1	0.18 ± 0.08	0.49 ± 0.3	0.43 ± 0.2
Fractional Intra-mechanism range	0.42 ± 0.03	1.21 ± 0.6	0.91 ± 0.8	1.28 ± 0.8

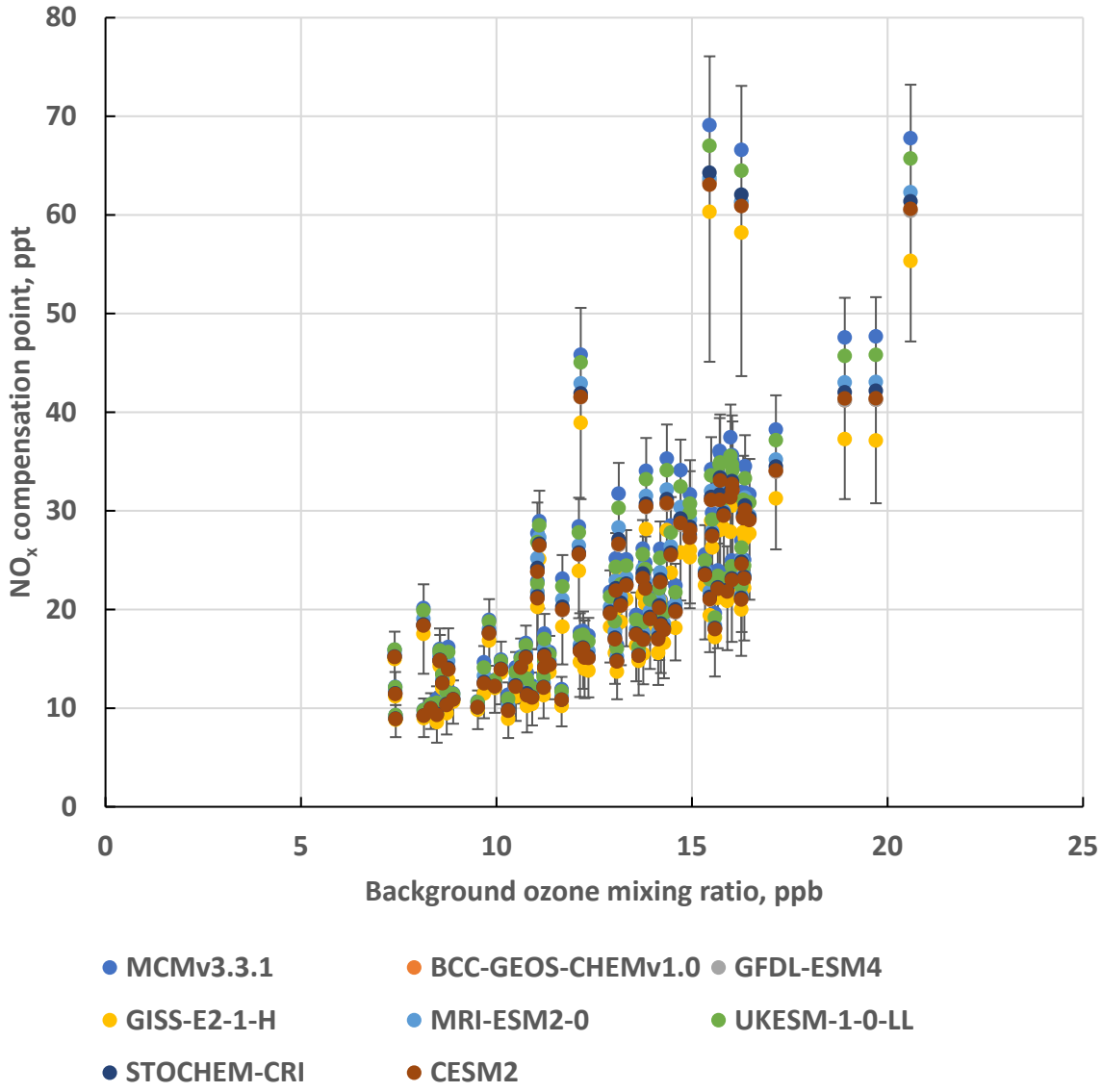

Figure 1. Scatter plot of the NO_x compensation points determined at each background location versus the background ozone mixing ratio for each model chemical mechanism. The error bars shown are for CESM2-WACCM based on the maximum and minimum values found in the Monte Carlo uncertainty analysis.

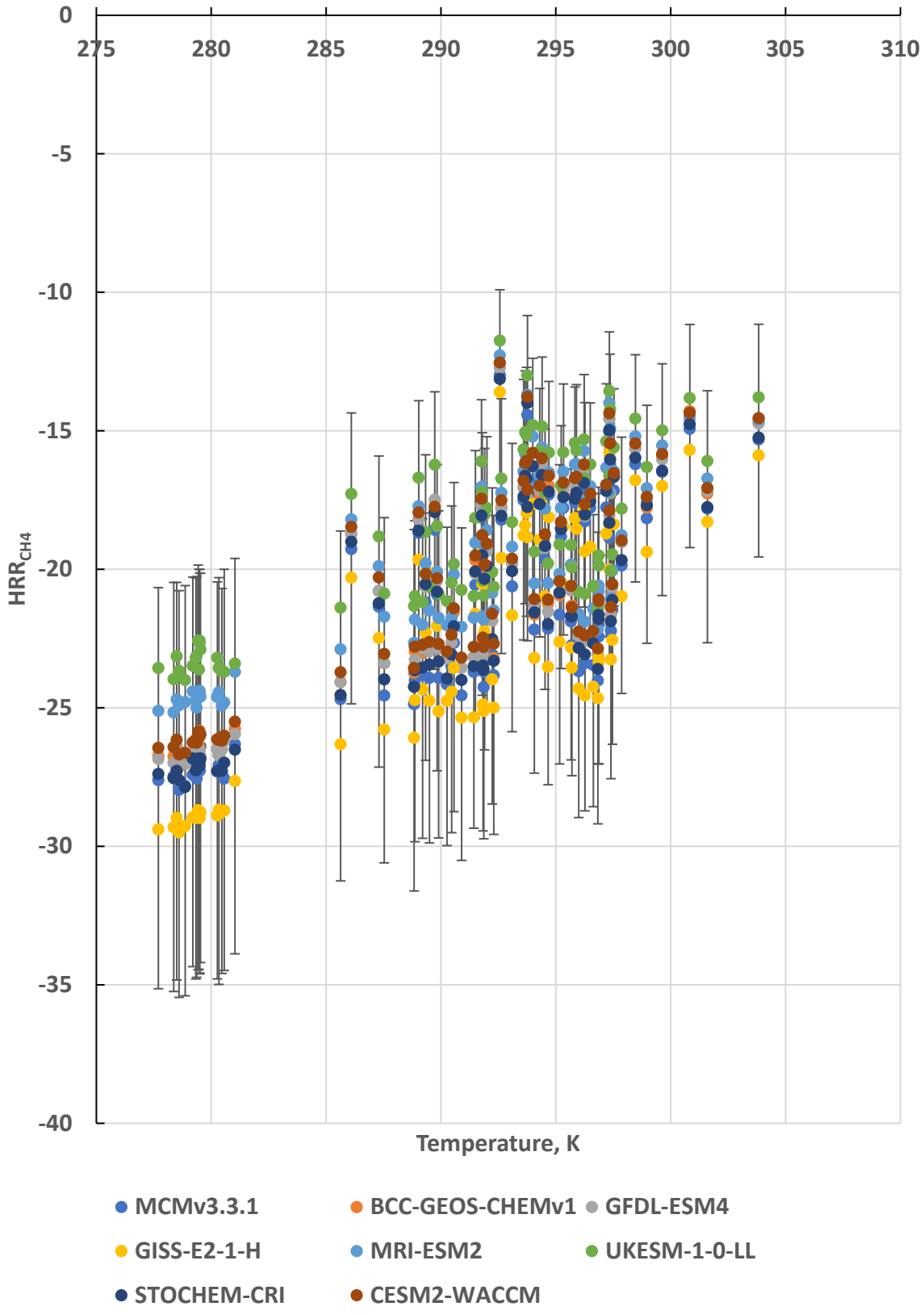

Figure 2. Scatter plot of the HRR_{CH4} values determined at each background location versus the background temperature for each model chemical mechanism. The error bars shown are for CESM2-WACCM based on the maximum and minimum values found in the Monte Carlo uncertainty analysis.

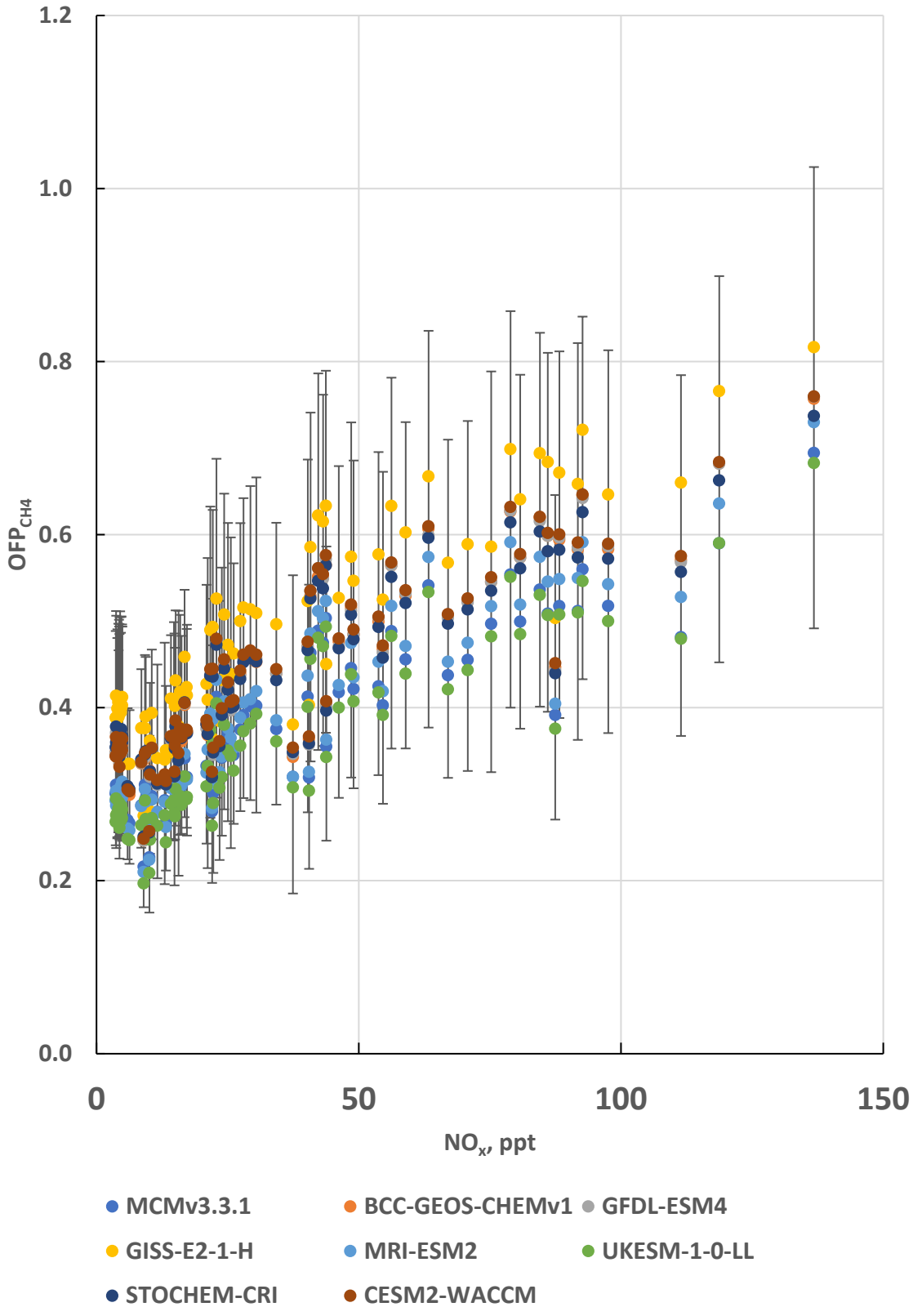

Figure 3. Scatter plot of the OFP_{CH4} values versus the background NO_x at each background location for each model chemical mechanism. The error bars shown are for CESM2-WACCM based on the maximum and minimum values found in the Monte Carlo uncertainty analysis.

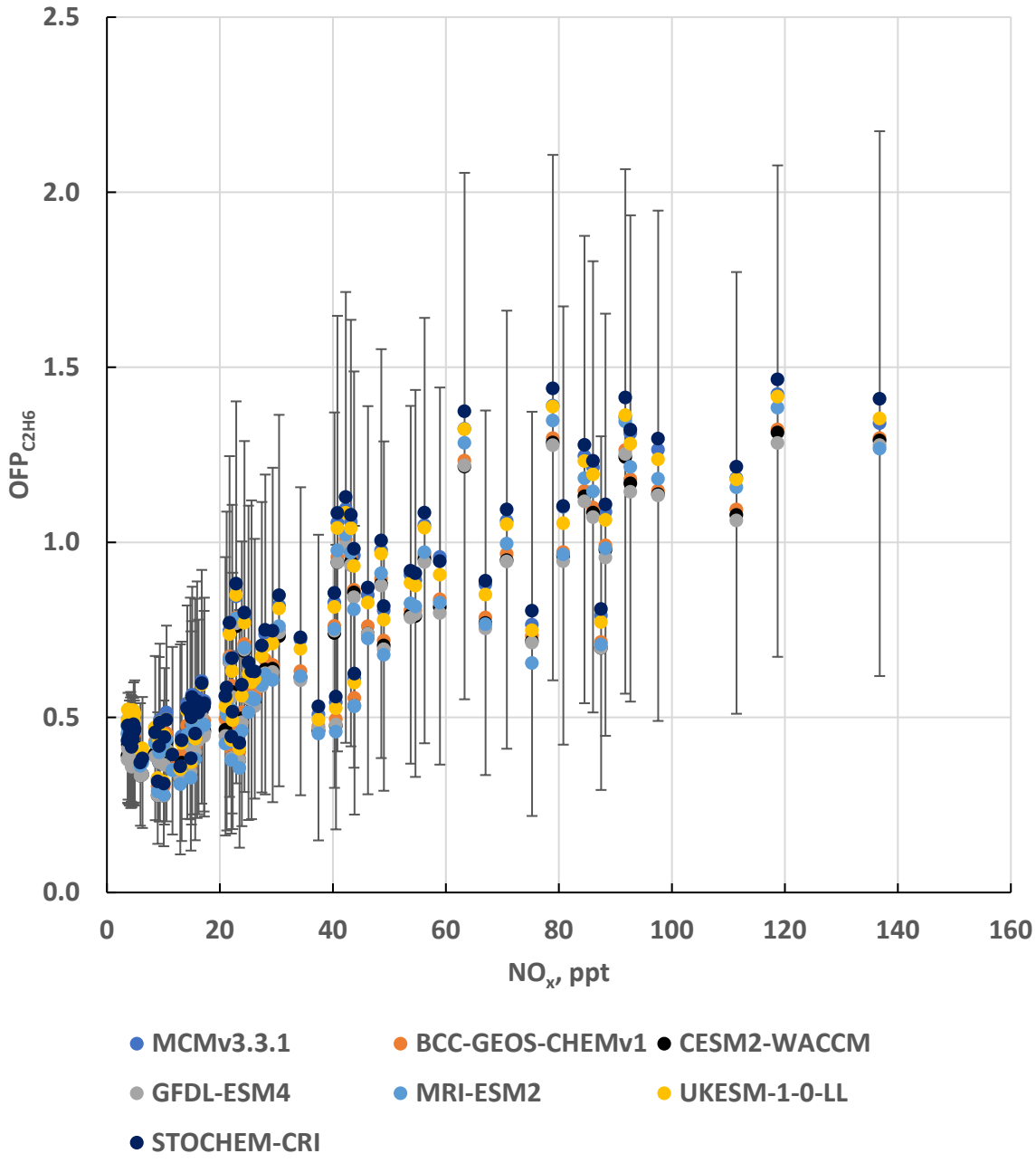

Figure 4. Scatter plot of the OFP_{C2H6} values versus the background NO_x at each background location for each model chemical mechanism. The error bars shown are for CESM2-WACCM based on the maximum and minimum values found in the Monte Carlo uncertainty analysis.

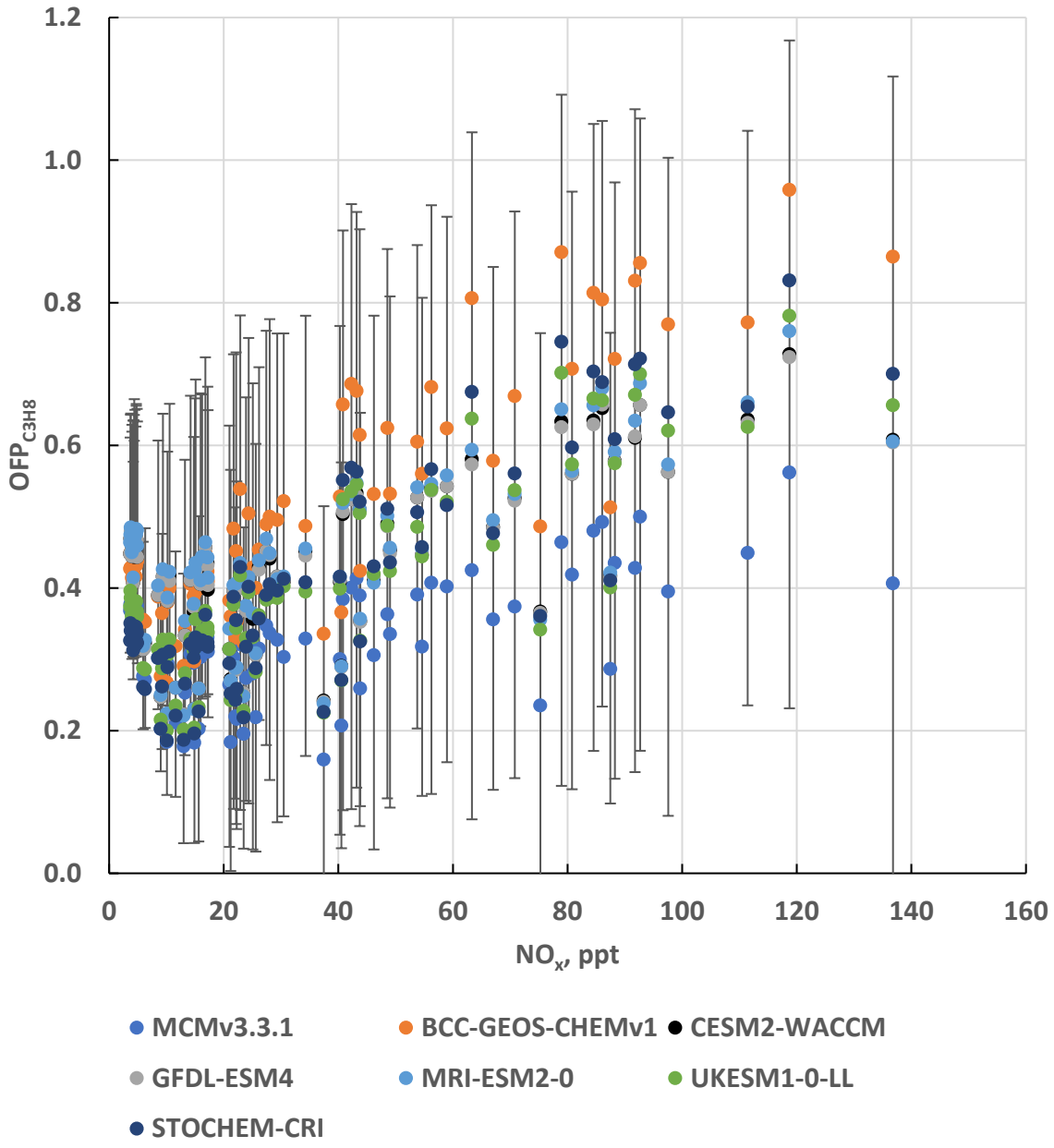

Figure 5. Scatter plot of the OFP_{C3H8} values versus the background NO_x at each background location for each model chemical mechanism. The error bars shown are for CESM2-WACCM based on the maximum and minimum values found in the Monte Carlo uncertainty analysis.

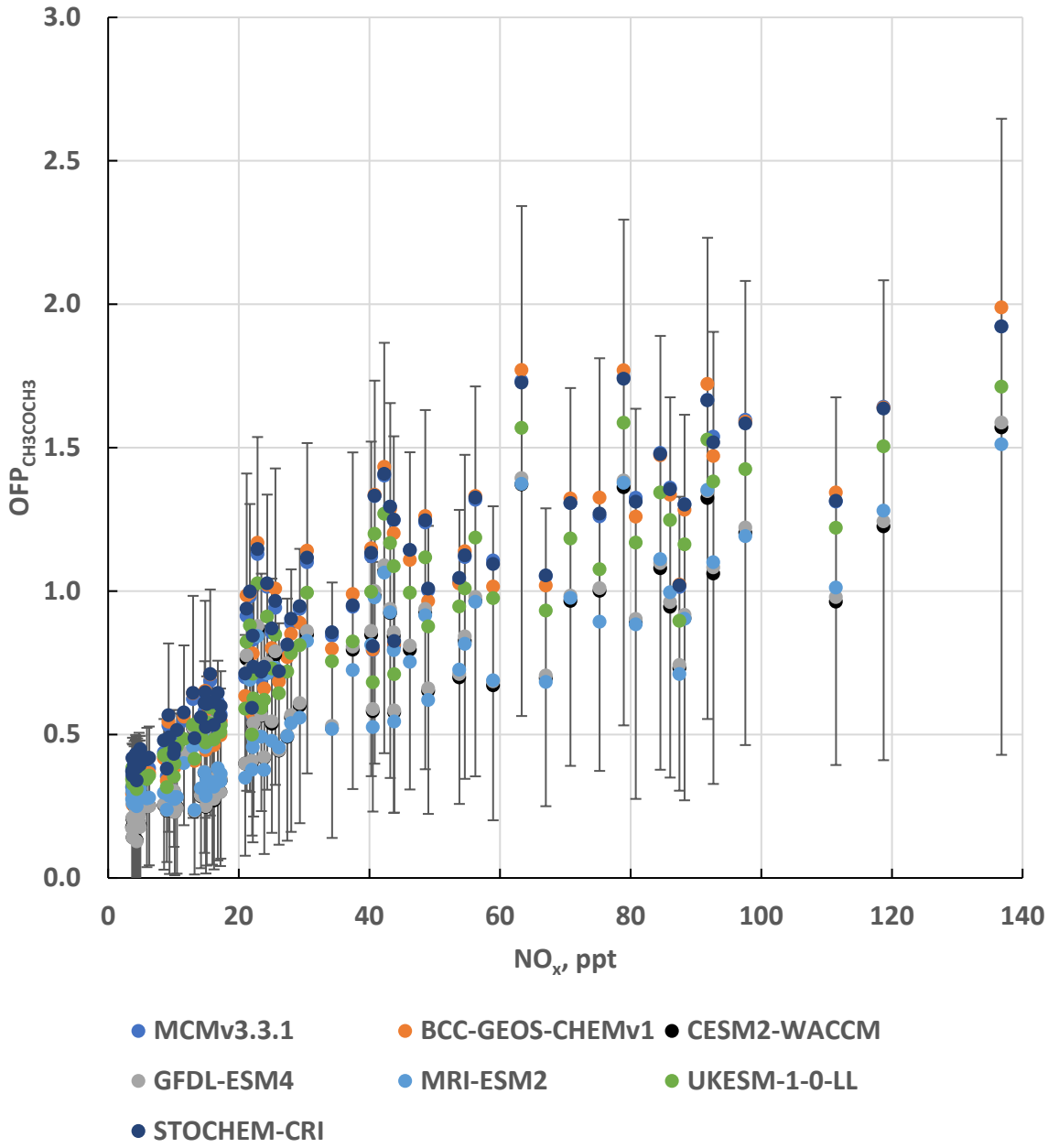

Figure 6. Scatter plot of the $OFP_{CH3COCH3}$ values versus the background NO_x at each background location for each model chemical mechanism. The error bars shown are for CESM2-WACCM based on the maximum and minimum values found in the Monte Carlo uncertainty analysis.